Geophysical Journal International

Geophys. J. Int. (2018) **213,** 1013–1028
Advance Access publication 2018 January 31
GJI Gravity, geodesy and tides

doi: 10.1093/gji/ggy033

Comparison of gravimetric and mantle flow solutions for sub-lithopsheric stress modeling and their combination

Mehdi Eshagh,[1] Bernhard Steinberger,[2,3] Robert Tenzer[4] and Andrés Tassara[5]

[1] *Department of Engineering Science, University West, SE-46186 Trollhättan, Sweden. E-mail: mehdi.eshagh@hv.se*
[2] *Helmholtz Centre Potsdam, GFZ German Research Centre for Geosciences, Telegrafenberg, D-*14473 *Potsdam, Germany*
[3] *Centre for Earth Evolution and Dynamics (CEED), University of Oslo, Postboks* 1028 *Blindern,* 0315 *Oslo, Norway*
[4] *Department of Land Surveying and Geo-Informatics, Hong Kong Polytechnic University,* 11 *Yuk Chai Rd, Hung Hom, Hong Kong*
[5] *Departamento de Ciencias de la Tierra, Facultad de Ciencias Químicas, Universidad de Concepción, Victor Lamas* 1290*, Concepción, Chile*

Accepted 2018 January 26. Received 2017 December 23; in original form 2017 August 03

SUMMARY

Based on Hager and O'Connell's solution to mantle flow equations, the stresses induced by mantle convection are determined using the density and viscosity structure in addition to topographic data and a plate velocity model. The solution to mantle flow equations requires the knowledge of mantle properties that are typically retrieved from seismic information. Large parts of the world are, however, not yet covered sufficiently by seismic surveys. An alternative method of modeling the stress field was introduced by Runcorn. He formulated a direct relation between the stress field and gravity data, while adopting several assumptions, particularly disregarding the toroidal mantle flow component and mantle viscosity variations. A possible way to overcome theoretical deficiencies of Runcorn's theory as well as some practical limitations of applying Hager and O'Connell's theory (in the absence of seismic data) is to combine these two methods. In this study, we apply a least-squares analysis to combine these two methods based on the gravity data inversion constraint on mantle flow equations. In particular, we use vertical gravity gradients from the Gravity field and steady state Ocean Circulation Explorer that are corrected for the gravitational contribution of crustal density heterogeneities prior to applying a localized gravity-gradient inversion. This gravitational contribution is estimated based on combining the Vening Meinesz-Moritz and flexural isostatic theories. Moreover, we treat the non-isostatic effect implicitly by applying a band-limited kernel of the integral equation during the inversion. In numerical studies of modeling, the stress field within the South American continental lithosphere we compare the results obtained after applying Runcorn and Hager and O'Connell's methods as well as their combination. The results show that, according to Hager and O'Connell's (mantle flow) solution, the maximum stress intensity is inferred under the northern Andes. Additional large stress anomalies are detected along the central and southern Andes, while stresses under most of old, stable cratonic formations are much less pronounced or absent. A prevailing stress-vector orientation realistically resembles a convergent mantle flow and downward currents under continental basins that separate Andean Orogeny from the Amazonian Shield and adjacent cratons. Runcorn's (gravimetric) solution, on the other hand, reflects a tectonic response of the lithosphere to mantle flow, with the maximum stress intensity detected along the subduction zone between the Nazca and Altiplano plates and along the convergent tectonic margin between the Altiplano and South American plates. The results also reveal a very close agreement between the results obtained from the combined and Hager and O'Connell's solutions.

Key words: Gravity anomalies and Earth structure; Loading of the Earth; Satellite gravity.

1 INTRODUCTION

The first low-degree global gravity models in the 1960s determined from orbital parameters of the early satellite missions were used, among other studies, to investigate the global mantle convection pattern and its relation with the global tectonic plate configuration and lithospheric stresses. Kaula (1963), for instance, developed a method based on minimizing the strain energy and using the

low-degree gravitational and topographic harmonics to estimate the minimum stresses in an elastic Earth. McKenzie (1967) studied heat flow in the mantle using gravity anomalies. Marsh & Marsh (1976) compiled a 2-D mantle convection model based on global gravity anomalies. Runcorn (1964, 1967) formulated a functional relation between the stress and gravity field based on solving the Navier–Stokes' equations for modeling the horizontal shear stresses in the mantle, while considering a two-layered model for the Earth, a lithosphere overlaying mantle of uniform viscosity. He then used the low-degree spherical harmonics of the Earth's gravity field to deduce the global horizontal stress pattern, and found a relation with convergent and divergent sites established by plate tectonic theory. Liu (1977, 1978) applied Runcorn's theory to construct maps of the convection-generated stresses driving movements of tectonic plates. McNutt (1980) used regional gravity data to interpret stresses within the crust and upper mantle. Fu & Huang (1983) extended Runcorn's definition for the full stress tensor. Ricard *et al.* (1984) investigated the connection between lithospheric stresses and geoid undulations. In a more recent study, Eshagh (2014) modified Runcorn's theory for the satellite-gradiometry data.

The direct modeling of mantle convection pattern or stresses solely from gravity data has no unique solution. Moreover, some objections were raised against using Runcorn's theory, particularly questioning approximations adopted in his formulation of the stress field. He, for instance, took into consideration only the poloidal flow component in the mantle, while disregarding the toroidal component. Phillips & Ivins (1979) argued that his theory could not realistically describe the actual global mantle convection pattern, because Runcorn assumed only a constant viscosity within the sub-lithospheric mantle. To overcome these theoretical deficiencies of Runcorn's theory, Hager & O'Connell (1981) solved for mantle flow by incorporating the plate velocity model, radially variable viscosity as well as both the poloidal and toroidal flows in the mantle. Steinberger *et al.* (2001) applied this method to investigate the global lithospheric stress pattern induced by a global mantle circulation, and Medvedev (2016) inferred the stress pattern within the African tectonic plate based on combining methods for modeling thermal isostasy and gravitational potential energy. Hager and O'Connell's solution based on mantle flow equations, however, requires information on mantle density anomalies that is typically inferred from seismic tomography. Ricard *et al.* (1984) and Richards & Hager (1984) suggested to use the global geoid model as information to constrain radial viscosity structure for solving Hager and O'Connell's theory. In this way, the gravity information is incorporated into the mantle flow solution. Following this idea, we proposed here a different approach that combines Runcorn (gravimetric) and Hager and O'Connell's (mantle flow) solutions by applying a least-squares approach to solve jointly both types of observation equations.

To enhance the mantle signature in gravity data used for modeling the stresses induced by mantle convection, the gravitational signal of crustal density heterogeneities should be removed. Some authors solve this problem by applying a spectral filtering or spectral decomposition. These methods, however, do not provide a unique solution, because the long-wavelength gravity spectrum comprises not only the gravitational signature of mantle density heterogeneities, but also a significant contribution from the crust. If a crustal density model is available, gravimetric forward modeling could be applied to remove the gravitational contribution of the crustal density structure (e.g. Tenzer *et al.* 2015). The refined gravity data corrected for the gravitational contribution of crustal density heterogeneities still comprise an additional gravitational signal that could not readily be modeled and removed based on applying the gravimetric forward modeling, because the isostatic balance depends on the loading and effective elastic thickness, rigidity and rheology of the lithosphere, and viscosity of the asthenosphere (Watts 2001). Moreover, glacial isostatic adjustment, present-day glacial melting, plate tectonics, mantle convection and other geodynamic processes contribute to the overall isostatic balance. To address these issues, we propose and apply an alternative method for modeling the gravitational contribution of crustal density structure based on combining the Vening Meinesz-Moritz's (VMM) and flexural isostatic theories. This is possible, because these two methods for the gravimetric Moho recovery are equivalent if the elastic lithosphere thickness and lateral crustal density variations are chosen appropriately. In this way, we can assume that both methods yield the same Moho result, thus can be combined in order to derive other parameters which are functionally related either to the VMM or flexural isostatic model. A similar principle was proposed already by Stewart & Watts (1997) and Braitenberg *et al.* (2002) in order to estimate the elastic thickness of the lithosphere. Theoretical foundations for combining these two isostatic theories were given by Eshagh (2016), who investigated their agreement for Moho modeling under the Tibetan Plateau. It is important to mention here that this combination can be applied only for the long-to-medium-wavelength topographic features and crustal density heterogeneities that are mostly in an isostatic equilibrium. This principle, however, does not hold for more detailed features, because loads shorter than 100 km are not isostatically compensated (e.g. Turcotte & Schubert 2014, p. 252). This corresponds to a spatial resolution of about 1 arcdeg, or a maximum degree of loading coefficients about 180 (e.g. Abrehdary 2016). Moreover, the isostatic equilibrium does not hold, for instance, along oceanic subduction zones. To address this issue, we used the gravity spectrum only up to spherical harmonic degree 31, corresponding to long wavelengths larger than 1200 km. The numerical investigations in this study were conducted within the South American continental lithosphere, where we compared the results of lithospheric stress modeling based on applying Runcorn's and Hager and O'Connell's methods and investigated a possibility of combining these two methods.

2 VMM AND FLEXURAL ISOSTATIC MODELS

In this section, we briefly summarize the VMM and flexural isostatic theories, before combining them for deriving the relation between the crustal density structure and its gravitational contribution in Section 3.

2.1 VMM model

Eshagh (2017) formulated the VMM problem for finding the Moho depth T from the gravity disturbances δg in the following spectral form

$$T = \frac{R}{3}\left[1-\left(1-\frac{T_0}{R}\right)^3\right] + \frac{1}{4\pi G\Delta\rho}\sum_{n=0}^{\infty}\left(\frac{2n+1}{n+1}\right)\beta_n{}^{-1} \times \sum_{m=-n}^{n}\left(\delta g_{nm}^{\mathrm{TB}} + \delta g_{nm}^{\mathrm{Sed}} + \delta g_{nm}^{\mathrm{Crys}} - \delta g_{nm}\right) Y_{nm}(\theta,\lambda), \quad (1a)$$

where T_0 is the mean Moho depth, R is the Earth's mean radius, G is Newton's gravitational constant, $\Delta\rho$ is the Moho density contrast and the parameter β_n is given by

$$\beta_n = \begin{cases} 1-(n+2)\,\frac{T_0}{2R} & \text{over continents} \\ 1 & \text{over oceans} \end{cases}. \tag{1b}$$

The gravity data used to compute the Moho depth according to eq. (1a) are corrected for the gravitational contributions of topography and density contrasts of bathymetry (i.e. the ocean density contrast), sediments and consolidated crust. These gravity data and gravity corrections are described by the corresponding spherical harmonics of the gravity disturbances δg_{nm} and the spherical harmonics of the gravitational contributions of topography/bathymetry $\delta g_{nm}^{\mathrm{TB}}$, sediments $\delta g_{nm}^{\mathrm{Sed}}$ and density heterogeneities within the consolidated crust $\delta g_{nm}^{\mathrm{Crys}}$.

Disregarding the terms $-{T_0}^2/R$ and $+{T_0}^3/R^2$ on the right-hand side of eq. (1a), the expression for computing the Moho depth correction ΔT was found to be (*cf.* Eshagh 2017)

$$\Delta T = \frac{1}{4\pi G\Delta\rho}\sum_{n=0}^{\infty}\left(\frac{2n+1}{n+1}\right)\left(1-(n+2)\,\frac{T_0}{2R}\right)^{-1} \times \sum_{m=-n}^{n}\left(\delta g_{nm}^{\mathrm{TB}}+\delta g_{nm}^{\mathrm{Sed}}+\delta g_{nm}^{\mathrm{Crys}}-\delta g_{nm}\right)Y_{nm}(\theta,\lambda). \tag{1c}$$

The Moho depth correction ΔT computed according to eq. (1c) is added to the mean value T_0 in order to obtain the gravimetric Moho depth; that is, $T = \Delta T + T_0$.

2.2 Flexural isostatic model

The assumption that the crust (corrected for anomalous density structures) is in an isostatic equilibrium is adopted for solving the VMM model (Sjöberg 2009) as described by eq. (1c). However, the original idea of Vening Meinesz (1931) was that the load of topographic mass is bending the lithosphere, while the bathymetric mass deficiency has an opposite effect. To describe mathematically a flexural deformation due to loading, the elastic shell theory can be adopted (*cf.* Kraus 1967, p. 156). Turcotte & Schubert (1982) studied the flexure of elastic lithosphere under the topographic load, while assuming a uniform lithospheric density structure. Here, we generalized their method for modeling the lithospheric flexure more realistically by taking into consideration the heterogeneous lithospheric density structure. Moreover, the load in partial differential equations that should be solved for computing the lithospheric flexure propagates directly to Moho undulations.

To begin with, we write the loading theory for an elastic lithospheric shell in the following form (Kraus 1967)

$$\left[\frac{D}{R^4}\left(\nabla^6+4\nabla^4\right)+\frac{ET_e}{R^2}\left(\nabla^2+2\right)\right]\Delta T+\left(\nabla^2+1-\nu\right) \times \Delta T\Delta\rho g=\left(\nabla^2+1-\nu\right)\bar{K}g, \tag{2a}$$

where g is the Earth's mean gravity at sea level, E is Young's modulus, T_e is the elastic thickness of the lithosphere, ν is Poisson's ratio, ∇ denotes the gradient operator and the parameter D of flexural rigidity is given by

$$D=\frac{ET_e^3}{12\left(1-\nu^2\right)}. \tag{2b}$$

We further define the density parameter $\bar{K}$ as follows

$$\bar{K}=\bar{\rho}H+\rho^{\mathrm{sed}}H^{\mathrm{sed}}+\rho^{\mathrm{Crys}}H^{\mathrm{Crys}}, \tag{2c}$$

where ρ^{sed} and H^{sed} are the density and thickness parameters of sediment layers, and the corresponding parameters ρ^{Crys} and H^{Crys} are defined for the consolidated crustal layers. The density distribution function $\bar{\rho}$ within the topography and bathymetry in eq. (2c) is defined as

$$\bar{\rho}=\begin{cases}\rho_{\mathrm{c}} & H\geq 0\\ \rho_{\mathrm{w}}-\rho_{\mathrm{c}} & H<0\end{cases}, \tag{2d}$$

where H is the topographic/bathymetric height, $\rho_{\mathrm{c}}=2670\ \mathrm{kg\ m^{-3}}$ is the topographic density and $\rho_{\mathrm{w}}=1027\ \mathrm{kg\ m^{-3}}$ is the sea water density (e.g. Gladkikh & Tenzer 2011).

Eshagh (2016) presented the solution of the differential equation in eq. (2a) in the following spectral form

$$\left[\frac{D}{R^4}\left(\kappa_n^3+4\kappa_n^2\right)+\frac{ET_e}{R^2}\left(\kappa_n^2+2\right)\right](\Delta T)_{nm}+\left(\kappa_n+1-\nu\right) \times(\Delta T)_{nm}\Delta\rho g=\left(\kappa_n+1-\nu\right)\bar{K}_{nm}g, \tag{2e}$$

where

$$\kappa_n^2=n^2(n+1)^2. \tag{2f}$$

We further rearrange the expression in eq. (2e) for computing the Moho depth correction as follows

$$\Delta T=\sum_{n=0}^{\infty}C_n\sum_{m=-n}^{n}\left(\bar{K}\right)_{nm}Y_{nm}(\theta,\lambda), \tag{2g}$$

with the parameter C_n given by

$$C_n=\frac{\kappa_n-(1-\nu)}{\left(\kappa_n^3-4\kappa_n^2\right)\frac{D}{R^4g}+\frac{ET_e}{R^2g}\left(\kappa_n-2\right)+\left(\kappa_n-(1-\nu)\right)\Delta\rho}. \tag{2h}$$

The expressions in eqs (1c) and (2h) describe two different methods for computing the Moho depth, but their solutions should theoretically be the same if the lithospheric shell is elastic, while an isostatic equilibrium exits in all regions globally. As stated in Section 1, the assumption of isostasy is also warranted, because in our solution we limited the spherical harmonic resolution up to the degree 31. We can then combine both theoretical models to derive a functional relation linking the crustal density structure and its gravitational contribution. To utilize the Gravity field and steady state Ocean Circulation Explorer (GOCE) data for solving this problem, we reformulated this functional relation in terms of the vertical gravitational gradient. These expressions are given in the next section.

3 LITHOSPHERIC MASS HETEROGENEITIES FROM COMBINING VMM AND FLEXURAL MODELS

Under the adopted assumption that both Moho solutions obtained by solving the VMM and flexural isostatic models in eqs (1c) and (2h) are identical, we could establish a direct mathematical model that functionally relates the crustal density structure with its gravitational contribution. This principle has been used, for instance, by Braitenberg *et al.* (2002) and Stewart & Watts (1997) to estimate the elastic thickness of the lithosphere. This assumption is generally valid in the absence of regional changes in the lithospheric configuration, but could be applied for studies of the lithospheric stress field based on the analysis of the long-to-medium-wavelength gravity spectrum. For this purpose, we generalized the functional model in eq. (2c) by means of crustal density heterogeneities. It is worth

mentioning here that density heterogeneities within the whole lithosphere could readily be included into this model either by applying an additional gravity correction due to subcrustal lithospheric density heterogeneities, or by assuming variable Moho density contrast, which implicitly incorporates lateral density variations in the subcrustal lithosphere. The former approach was applied in this study. We have used the CRUST1.0 seismic model to compute the gravitational contribution of crustal density heterogeneities, meaning that the flexural and VMM Moho results are inherently constrained by this seismic model.

To derive the functional relation between the crustal density structure and its contribution to the vertical gravity gradient (i.e. the second-order radial derivative of the disturbing potential), we first write a functional relation between the spherical harmonics of the gravity disturbance δg_{nm} and the corresponding spherical harmonics of the vertical gravity gradient $V_{rr,nm}$as follows (*cf.* Eshagh & Hussain 2016)

$$\delta g_{nm} = \frac{R}{n+2}\frac{1}{s^{n+3}}V_{rr,nm},\quad S=\frac{R}{r}. \tag{3a}$$

After applying the functional relation between δg_{nm} and $V_{rr,nm}$ to gravity corrections defined in eq. (1a), we get

$$(\Delta T)_{nm} = \frac{R}{4\pi G\Delta\rho}\frac{(2n+1)}{(n+1)(n+2)}\beta_n{}^{-1}s^{-n-3} \times \left(V_{rr,nm}^{\mathrm{TB}} + V_{rr,nm}^{\mathrm{Sed}} + V_{rr,nm}^{\mathrm{Crys}} - V_{rr,nm}\right), \tag{3b}$$

where $V_{rr,nm}^{\mathrm{TB}}$, $V_{rr,nm}^{\mathrm{Sed}}$ and $V_{rr,nm}^{\mathrm{Crys}}$ are, respectively, the gravity-gradient corrections due to topography/bathymetry, sediments and consolidated crust.

Combining eqs (2g) and (3b), solving the result for $V_{rr,n}$, and applying summations (for n and m) on both sides of eq. (3b), we finally arrive at

$$-\frac{4\pi G\Delta\rho}{R}\sum_{n=0}^{\infty}\frac{(n+1)(n+2)}{(2n+1)}\beta_n s^{n+3}C_n\sum_{m=-n}^{n}\left(\bar{K}\right)_{nm}Y_{nm}(\theta,\lambda) + \left(V_{rr}^{\mathrm{TB}} + V_{rr}^{\mathrm{Sed}} + V_{rr}^{\mathrm{Crys}}\right) = V_{rr}^{\mathrm{crust}}. \tag{3c}$$

The expression in eq. (3c) describes the contribution of crustal density heterogeneities on the vertical gravity gradient. We emphasized this by introducing the notation V_{rr}^{crust} instead of V_{rr}.

4 LITHOSPHERIC STRESS FROM GRAVITY DATA

Runcorn (1967) assumed a two-layered model of the Earth, and developed a theory for Newtonian constant-viscosity Stokes' flow to correlate the gravity field with the global mantle convection pattern. He explicitly related the gravity potential to a volume integral of the poloidal velocity function and through application of Green's theorem, further transformed this functional relation after several approximations to surface integrals over the inner and outer boundaries of the spherical shell of the assumed Earth's model (*cf.* Runcorn 1967, Phillips & Ivins 1979). Based on these assumptions, he introduced the lithospheric shear stress components in the following spectral form

$$S_{r\theta} = \kappa\sum_{n=2}^{\infty}\frac{2n+1}{n+1}\left(\frac{R}{R-D}\right)^{n+1}\sum_{m=-n}^{n}V_{nm}\frac{\partial Y_{nm}(\theta,\lambda)}{\partial\theta}, \tag{4a}$$

and

$$S_{r\lambda} = \kappa\sum_{n=2}^{\infty}\frac{2n+1}{n+1}\left(\frac{R}{R-D}\right)^{n+1}\sum_{m=-n}^{n}V_{nm}\frac{\partial Y_{nm}(\theta,\lambda)}{\sin\theta\,\partial\lambda}, \tag{4b}$$

where V_{nm} are the spherical harmonics of the disturbing potential, and D denotes the mean depth of the lithospheric base (i.e. the lithosphere–asthenosphere boundary). The parameter κ in eq. (4b) reads

$$\kappa = \frac{Mg}{4\pi(R-D)^2}, \tag{4c}$$

where M is the total mass of the Earth (including its atmosphere).

Eshagh (2014) reformulated Runcorn's theory so that the stress-generating function S_r is defined as a function of spherical harmonics instead of their partial derivatives (see eqs 4a and 4b). Hence, we have

$$S_r = \kappa\sum_{n=2}^{\infty}\frac{2n+1}{n+1}\left(\frac{R}{R-D}\right)^{n+1}\sum_{m=-n}^{n}V_{nm}Y_{nm}(\theta,\lambda). \tag{4d}$$

In this way, the stress-generating function S_r is first computed according to eq. (4d), and the northward and eastward stress components $S_{r\theta}$ and $S_{r\lambda}$ are then obtained from the stress-generating function S_r by applying a numerical differentiation. The idea behind applying this modification, instead of using original formulae given by Runcorn, was to improve the spectral resolution due to the divergence of an asymptotically convergent series in eqs (4a) and (4b). Moreover, the stress-generating function (in eq. 4d) defined in terms of the gravitational potential represents the most generic form, suitable for deriving the stress field as a function of any type of gravity field quantities, such as the geoid undulations, gravity, deflections of the vertical, or gravity-gradient components. The integral equation that links the vertical gravity gradient V_{rr} with the stress-generating function S_r is then defined by

$$\frac{1}{4\pi\kappa(R-D)^2}\iint_{\sigma}K(k,\psi)\,S_r\,\mathrm{d}\sigma = V_{rr} - V_{rr}^{\mathrm{crust}}, \tag{4e}$$

where σ is the unit sphere, and $\mathrm{d}\sigma$ is the surface integration element. The kernel function K in eq. (4a) reads

$$K(k,\psi) = \sum_{n=2}^{\infty}(n+1)^2(n+2)\,k^{n+3}P_n(\cos\psi),\ k=\frac{R-D}{r}, \tag{4f}$$

where $P_n(\cos\psi)$ denotes the Legendre polynomial of degree n for the argument of the spherical angle ψ between the computation and integration points, and r is the geocentric distance.

5 LITHOSPHERIC STRESS FROM PLATE MOTIONS AND MANTLE FLOW

In principle, the lithospheric stresses induced by mantle convection can be derived from large-scale mantle flow and plate motions. The motion and geometry of tectonic plates represent the boundary conditions for a mantle circulation pattern. By assuming radially variable Newtonian viscosity, and 3-D mantle density anomalies, the mantle flow can be determined analytically. Stresses induced by mantle flow can then be expressed in the following form (Steinberger *et al.* 2001)

$$S_{rr} = \sum_{n=0}^{\infty}\sum_{m=-n}^{n}S_{rr,nm}Y_{nm}(\theta,\lambda), \tag{5a}$$

$$S_{r\theta} = \sum_{n=0}^{\infty} \sum_{m=-n}^{n} \left(S_{\mathrm{p},nm} \frac{\partial Y_{nm}(\theta,\lambda)}{\partial \theta} + S_{\mathrm{t},nm} \frac{\partial Y_{nm}(\theta,\lambda)}{\sin\theta \partial \lambda} \right), \tag{5b}$$

and

$$S_{r\lambda} = \sum_{n=0}^{\infty} \sum_{m=-n}^{n} \left(S_{\mathrm{p},nm} \frac{\partial Y_{nm}(\theta,\lambda)}{\sin\theta \partial \lambda} - S_{\mathrm{t},nm} \frac{\partial Y_{nm}(\theta,\lambda)}{\partial \theta} \right), \tag{5c}$$

where $S_{\mathrm{p},nm}$ and $S_{\mathrm{t},nm}$ are the poloidal and toroidal spherical harmonics of the stress field, respectively. These stress components can be computed directly from the flow calculation according to the theory of Hager & O'Connell (1981), which reduces the spherical harmonic expansion of mantle flow to a set of ordinary differential equations. For more details, we refer readers to Steinberger *et al.* (2001).

As follows from eqs (4a) and (4b), and (5b) and (5c), the shear stresses induced by mantle convection can be derived by applying two independent methods and using two different data types. As mentioned above, Runcorn (1967) oversimplified the mantle rheology in order to find a direct mathematical relation between the gravity field and the lithospheric stresses. By comparing eq. (5b) with eq. (4a) and eq. (5c) with eq. (4b), we can see that the toroidal component of mantle circulation is absent in Runcorn's definition. Obviously, Runcorn (1967) clarified that the stresses presented in eqs (4a) and (4b) ignore the toroidal component. In fact, Runcorn mentioned that

$$S_{\mathrm{p},nm} = \kappa \frac{2n+1}{n+1} \left(\frac{R}{R-D} \right)^{n+1} V_{nm}, \quad \text{for } n \geq 2. \tag{5d}$$

So far, we briefly summarized two methods for modeling the stress field based on the gravity and mantle flow information. As stated above, Runcorn's method for modeling the stress field solely from gravity data does not provide a unique solution without using additional geophysical constraints. The mantle flow solution according to Hager and O'Connell, on the other hand, requires the knowledge of mantle rheology as well as mantle density heterogeneities, which might be restricted by the absence of seismic data over large parts of the world. It is thus natural to combine these two methods in order to find a solution for modeling the stress field. In the next section, we present a combination of the two methods by means of applying the least-squares analysis.

6 SOLUTION OF INTEGRAL EQUATIONS AND THEIR COMBINATION

To define the combined solution for stress field modeling, we formulate the functional relations that incorporate the equations for finding the stress-generating function from the gravity-gradient data and from the mantle flow equations. Obviously, the gravity-gradient data used for this purpose are corrected for the gravitational contribution of crustal density heterogeneities in order to extract the gravitational signature of the mantle (Section 3).

6.1 Stress-generating function

The integral equation in eq. (4e) relates the vertical gravity gradient V_{rr} with the stress-generating function S_r. Optimally, the number of input data should exceed the number of estimated values S_r. Such an overdetermined system can then be written as the Gauss–Markov adjustment model in the following form

$$\mathbf{A}\mathbf{s}_r = \mathbf{L} - \varepsilon, \ \mathrm{E}\left\{\varepsilon\varepsilon^{\mathrm{T}}\right\} = \sigma_0^2 \mathbf{Q}, \quad \text{and} \quad \mathrm{E}\{\varepsilon\} = 0, \tag{6a}$$

where $\mathbf{A}$ is the coefficient matrix of the system, which is derived after discretization of the integral in eq. (4e) according to the resolution of parameters being recovered, $\mathbf{L}$ is the observation vector containing V_{rr} with $\boldsymbol{\varepsilon}$ as their errors and $(.)^{\mathrm{T}}$ denotes a transposition operator. The vector of unknown parameters $\mathbf{s}_r$ is formed by values of S_r over the recovery area. The *a priori* variance factor σ_0^2 is set equal to 1, $\mathbf{Q} = \mathbf{I}$ is the positive definite cofactor matrix of the observations and $\mathrm{E}\{.\}$ denotes a statistical expectation. Eq. (6a) shows that the statistical expectation of the observation noise is zero, and its quadratic form defines the variance–covariance matrix of measurements. This means that data noise is random and follows Gaussian distribution. The integral equations in eq. (4e) after discretization form the observation equations that define a functional relation between the observed values V_{rr} and the unknown (and sought) values of S_r. Therefore, the number of equations is equal to the number of measurements or the number of rows in the matrix $\mathbf{A}$, and the number of S_r equals to the number of columns in $\mathbf{A}$.

Since the system of equations in eq. (6a) is ill-conditioned, Tikhonov's (1963) regularization is applied based on minimizing the following objective function

$$\min\left(\|\mathbf{A}\mathbf{s}_r - \mathbf{L}\|_2 + \alpha^2 \|\mathbf{s}_r\|_2 \right), \tag{6b}$$

where $\| \bullet \|_2$ denotes the L_2 norm, and α^2 is the regularization parameter.

The regularized solution of eq. (6b) that comprises the estimated values of S_r and the vector $\mathbf{L}$ formed by the gravity-gradient data (corrected for the gravitational contribution of crustal/lithospheric density heterogeneities) reads

$$\mathbf{s}_r = \left(\mathbf{A}^{\mathrm{T}}\mathbf{A} + \alpha^2 \mathbf{I} \right)^{-1} \mathbf{A}^{\mathrm{T}}\mathbf{L}. \tag{6c}$$

As explained above, Runcon's theory produces the shear stress components, which are the northward and eastward derivatives of S_r. Such a process can be described mathematically as follows

$$\frac{\partial S_r}{\partial \theta} = S_{r\theta}, \tag{6d}$$

$$\frac{\partial S_r}{\sin\theta \partial \lambda} = S_{r\lambda}, \tag{6e}$$

where $S_{r\theta}$ and $S_{r\lambda}$ are the northward and eastward stress components.

The values of the stress-generating function (S_r) form elements of the estimated vector $\mathbf{s}_r$. According to the chosen resolution for a stress recovery and the size of area, S_r can be presented in a matrix or grid form. Therefore, taking these derivatives numerically according to values of these functions on a grid and the distance between them is rather straightforward. For the vector $\mathbf{s}_r$, eqs (6d) and (6e) can be rewritten into the following vector-matrix form

$$\mathbf{s}_{r\theta} = \mathbf{B}\mathbf{s}_r, \tag{6f}$$

$$\mathbf{s}_{r\lambda} = \mathbf{D}\mathbf{s}_r, \tag{6g}$$

where $\mathbf{B}$ and $\mathbf{D}$ are the matrix operators for the conversion of the stress-generating functions S_r to the stress components $S_{r\theta}$ and $S_{r\lambda}$ that form the vectors $\mathbf{s}_{r\theta}$ and $\mathbf{s}_{r\lambda}$. In other words, they are matrices, which subtract each two adjacent values on a grid and divide this

difference by a distance between them. The matrix **B** operates on the columns of the grid and represents the northward derivatives, and **D** on the rows and eastward.

6.2 Stress-generating function from GOCE and mantle flow model

We further incorporated the stresses generated from the mantle flow model into the gravity-gradient data inversion. However, the mantle flow models are defined in terms of the northward and eastward shear stress components instead of the stress-generating function S_r, which is obtained from the gravity-gradient data inversion. Therefore, in order to perform a joint inversion, the system of equations should be constructed in such a way that the unknowns are either S_r or the shear stress components. However, since V_{rr} is used in this study, it is better to have the system for estimating S_r, otherwise, the kernel of the integral equation will be off bell-shaped and inappropriate for a local inversion. In this case, the matrix **A** and the vector **L** remain the same as defined in the previous section. Nevertheless, the shear stress components derived from the mantle flow model play roles of additional measurements to our system of equations. This means that the mathematical relation between S_r and these stresses should be established in such a way that by solving the system the values of S_r are derived from both, the gravity-gradient data as well as from the shear stress components of the mantle flow solution. Here, we assumed that the noise in all measurements is random. We further assumed that the weights of all measurements are equal. We then write

$$\begin{bmatrix}\mathbf{A}\\ \mathbf{B}\\ \mathbf{D}\end{bmatrix}\mathbf{s}_r^* = \begin{bmatrix}\mathbf{L}\\ \mathbf{s}_{r\theta}\\ \mathbf{s}_{r\lambda}\end{bmatrix} - \begin{bmatrix}\varepsilon_{\mathbf{L}}\\ \varepsilon_{\mathbf{s}_{r\theta}}\\ \varepsilon_{\mathbf{s}_{r\lambda}}\end{bmatrix},\ \mathrm{E}\{\varepsilon_{\mathbf{L}}\} = \mathrm{E}\left\{\varepsilon_{\mathbf{s}_{r\theta}}\right\} = \mathrm{E}\left\{\varepsilon_{\mathbf{s}_{r\lambda}}\right\} = 0,$$

and

$$\mathrm{E}\left\{\varepsilon_{\mathbf{L}}{\varepsilon_{\mathbf{L}}}^{\mathrm{T}}\right\} = \mathrm{E}\left\{\varepsilon_{\mathbf{s}_{r\theta}}\varepsilon_{\mathbf{s}_{r\theta}}^{\mathrm{T}}\right\} = \mathrm{E}\left\{\varepsilon_{\mathbf{s}_{r\lambda}}\varepsilon_{\mathbf{s}_{r\lambda}}^{\mathrm{T}}\right\} = \sigma_0^2\mathbf{I}, \tag{6h}$$

where the vector $\varepsilon_{\mathbf{L}}$ comprises errors of the gravity-gradient data in **L**, and the vectors$\varepsilon_{\mathbf{s}_{r\theta}}$ and $\varepsilon_{\mathbf{s}_{r\lambda}}$ comprise errors of the stress-vector components $\mathbf{s}_{r\theta}$ and $\mathbf{s}_{r\lambda}$ that are derived from a mantle flow model.

By adding eqs (6f) and (6g) into the system of equations in eq. (6a), the instability problem of the system is solved without a regularization. The least-squares estimate for $\hat{\mathbf{s}}_r^*$ in eq. (6h) is then described by:

$$\hat{\mathbf{s}}_r^* = \left(\mathbf{A}^{\mathrm{T}}\mathbf{A} + \mathbf{B}^{\mathrm{T}}\mathbf{B} + \mathbf{D}^{\mathrm{T}}\mathbf{D}\right)^{-1}\left(\mathbf{A}^{\mathrm{T}}\mathbf{L} + \mathbf{B}^{\mathrm{T}}\mathbf{s}_{r\theta} + \mathbf{D}^{\mathrm{T}}\mathbf{s}_{r\lambda}\right). \tag{6i}$$

As seen in eq. (6i), no weighting scheme has been considered in the solution. This means that each value of the stress component of the flow model has the same weight as that attributed to each value of the gravity gradient. The structure of **A**, **B** and **D** matrices thus determine the contribution of **L**,$\mathbf{s}_{r\theta}$ and $\mathbf{s}_{r\lambda}$ to the final joint solution of $\hat{\mathbf{s}}_r^*$. As demonstrated numerically, since the matrix **A** is ill-conditioned, the gravity-gradient data have weaker influence onto the final solution. The equations related to the shear stress components from the mantle flow model then dominate the solution, even if the number of gravity-gradient data used for the inversion is much higher. Finally, it is worth mentioning here that the system in eq. (6i) defines the least-squares solution for S_r, instead of directly for the stress components. In order to obtain a joint solution for the shear stress components, $\mathbf{s}_r$ should be replaced by $\hat{\mathbf{s}}_r^*$ in eqs (6f) and (6g) and the matrices **B** and **D** take the northwards and eastwards derivatives of it.

7 STUDY AREA AND DATA ACQUISITION

In this section, we briefly discuss the geological setting of study area comprising South America and then present input data and models used for computing the stress field according to theoretical models summarized in Sections 4–6.

7.1 Study area

The eastern part of South America (see Fig. 1) is formed by the Archaean to Palaeoproterozoic cratons (Amazonia, Sao Francisco, Rio de la Plata) that are separated from each other by the Mesoproterozoic to Neoproterozoic mobile belts associated with the amalgamation of Gondwana (e.g. Cordani & Sato 1999). The Transbrasiliano Lineament suture that is associated with one of the seismically active belts (Assumpçao *et al.* 2004) extends from the northwest and continues southwards. During the Phanerozoic some of the regions between the Precambrian fragments became the centre of intracontinental basins (Amazon and Paraná), later modified by flood basalt volcanism during the Mesozoic contemporaneous with the rifting between South America and Africa and the opening of the Atlantic Ocean. The western part of South America is characterized by the accretion of terrains to Gondwanaland during the Early Palaeozoic, the construction and collapse of a Late Palaeozoic subduction orogen, and the ongoing construction of another orogen since the Jurassic that is dominated by east-directed subduction of the Pacific oceanic lithosphere (e.g. Ramos 1999). The acceleration of the South American tectonic plate westwards resulted in compressive deformations along the convergent margin that forms the Andes. This area witnesses a strong along-strike morphological segmentation characterized by oroclinal bending of the Altiplano–Puna plateau. Bird (2003), analysing seismic and geodetic data, proposed the existence of separated tectonic blocks of Panamá, Northern Andes and Altiplano, which are moving more or less as rigid blocks relative to the South American plate. The eastern boundary of the Altiplano plate corresponds to the active margin of the Sierras Subandinas thrust-fold belt, and the northern and southern ones gradate to zones of diffuse crustal deformation. The southern part of South America formed by the Patagonian Platform is a geologically distinct lithospheric block with respect to the rest of the continent (e.g. Ramos 1999). Spreading centres between the Nazca, Cocos and Antarctic plates are subducted in the Andean trench, whereas the age of the Nazca plate increases towards the Central Andes, reaching a maximum of 45 My (Müller *et al.* 1997).

7.2 Input data

The data sets and models used for computations comprised the GOCE gravity-gradient data, the SRTM30 topographic/bathymetric model (Farr *et al.* 2007), the CRUST1.0 global seismic crustal model (Laske *et al.* 2013) and the elastic thickness model compiled by Tassara *et al.* (2007).

7.2.1 GOCE data

We used the GOCE satellite data over the study area observed during 2013 January with a 10 s data-sampling interval to compute the vertical gravity gradient (in total 21920 values) corrected for the normal gravity-gradient component according to the GRS80

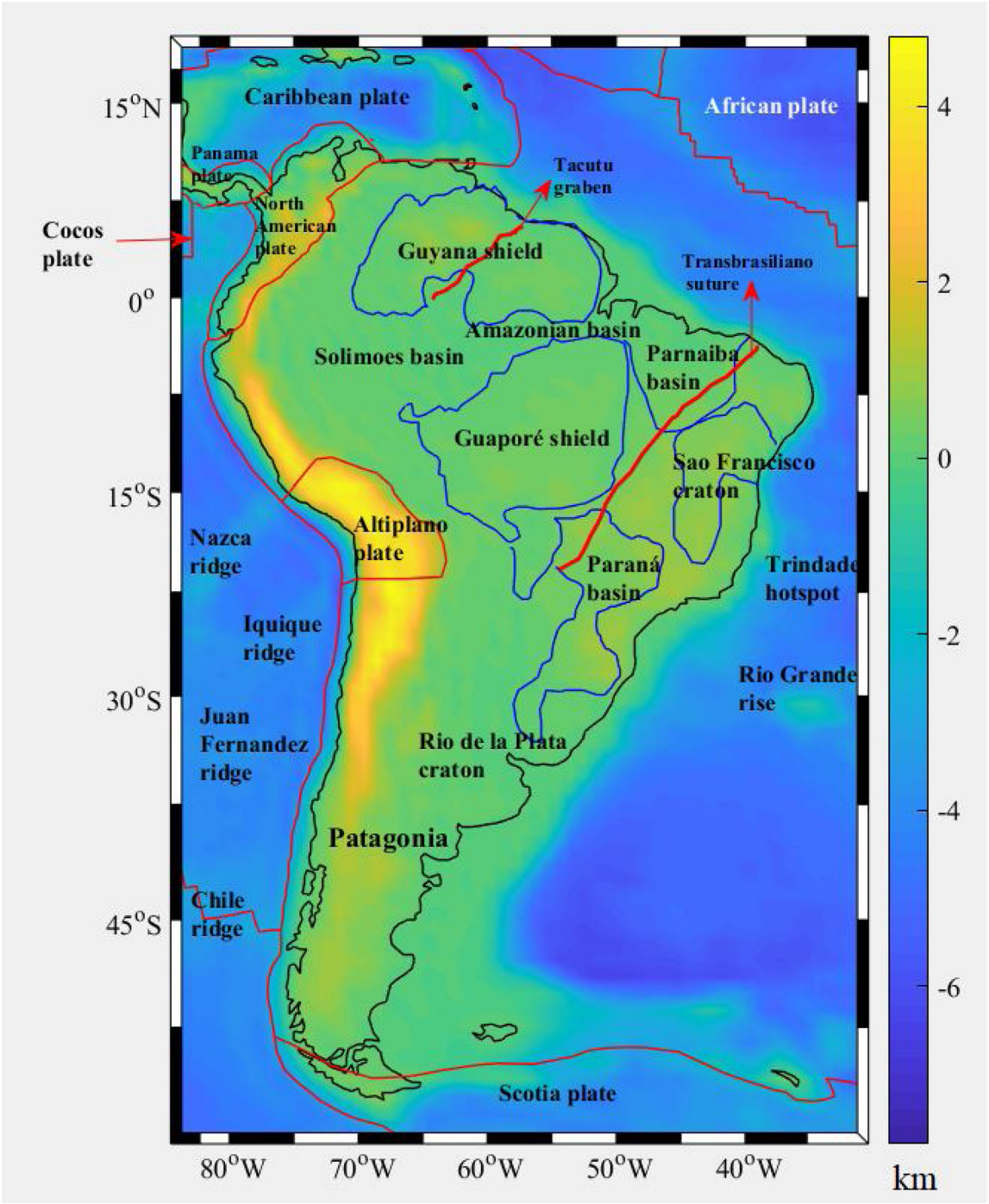

Figure 1. Geotectonic setting of South America. Tectonic plate boundaries are marked by red lines. The map also shows solid Earth topography.

parameters (Moritz 2000). Since we used only the long-wavelength gravity spectrum up to the spherical harmonic degree 31 that is not detected sufficiently by the GOCE gravity gradiometry, it is important to emphasize here that the GOCE Level 2 products have improved long-to-medium gravity spectrum. This is assured by using a global gravity model during the transformation of GOCE observables from the gradiometer frame to the local north-oriented frame, with subsequent filtering of GOCE data with high-pass filters, replacing low frequencies by GOCE-QL model, and incorporating the reduced dynamic orbit of GOCE into the solution (see GOCE Level 2 Product Data Handbook).

As seen in Fig. 2, large positive values of vertical gravity gradient are distributed along Andes with maxima (up to 1.5 E) in its central part. The largest negative values mark locations of the oceanic subductions along the Puerto Rico and Peru-Chile trenches. Elsewhere, the values are typically within the interval of ±0.5 E.

7.2.2 CRUST1.0

We used 1 × 1 arcdeg data from CRUST1.0 to compute the variable Moho density contrast. This density contrast was computed as the

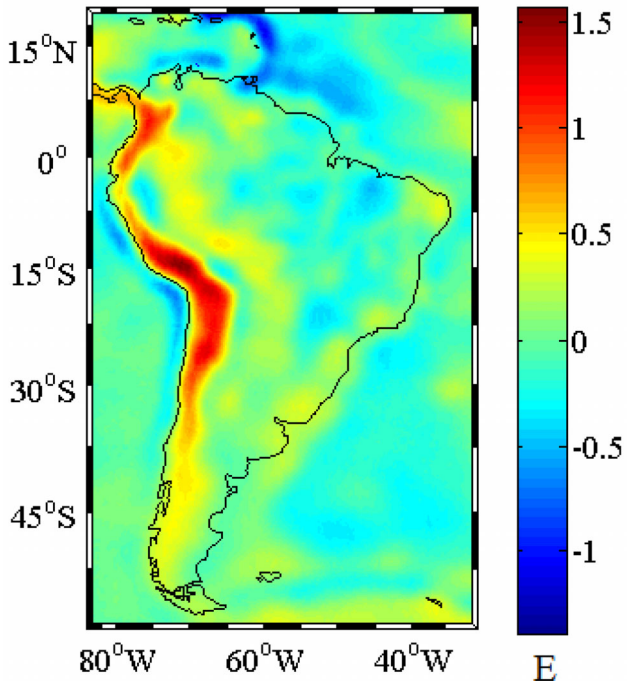

Figure 2. Regional map of the vertical gravity gradient.

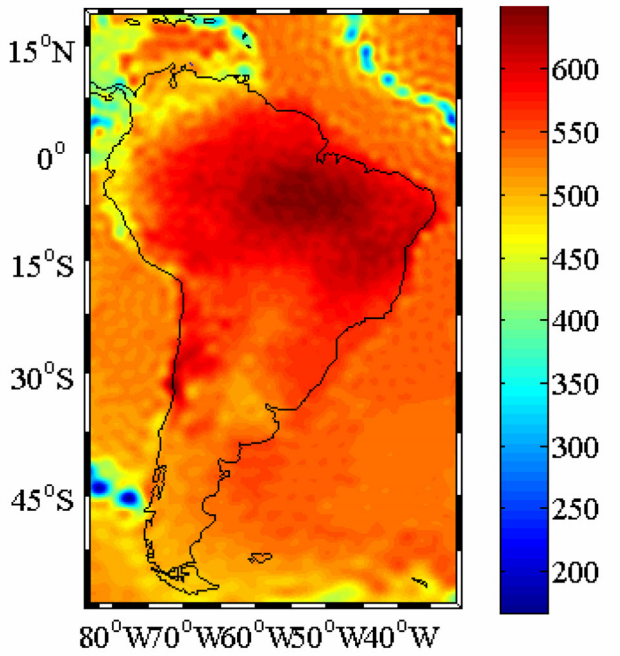

Figure 3. Moho density contrast (kg m^{-3}).

difference between the uppermost mantle density and the average crustal density evaluated as the weighted mean of density values within the CRUST1.0 layers according to the thickness of each layer. The Moho density contrast is shown in Fig. 3. Maxima, exceeding 600 kg m^{-3}, agree with locations of the Brazilian Shield and São FranciscoCraton, and minima are typically along the mid-oceanic ridges. A relatively small Moho density contrast is also detected along the oceanic subduction under the Puerto Rico Trench, while such a feature is absent along the Peru-Chile trench.

7.2.3 Gravity-gradient corrections

We further computed the gravity-gradient corrections due to topography, bathymetry, sediments and consolidated crust, and applied them to the GOCE vertical gravity gradients. The computation was realized according to the procedure developed by Tenzer *et al.* (2012) which utilizes methods for a spherical harmonic analysis and synthesis of the gravity and crustal structure data (see also Rexer *et al.* 2016). The combined topographic/bathymetric correction was computed using the SRTM30 data for the average density of the upper continent crust 2670 kg m^{-3} (Hinze 2003). The same density value was adopted to define the density contrasts for the stripping gravity-gradient corrections. The sediment and consolidated crust corrections were computed from the 1 × 1 arcdeg CRUST1.0 data. The results are shown in Fig. 4.

The combined contribution of topography and bathymetry on the vertical gravitational gradient (Fig. 4a) is typically negative offshore while positive inland, with maxima in central Andes exceeding 6 E. The sediment contribution (Fig. 4b) is typically within the interval ±0.5 E, except for large negative values along continental margins characterized by significant marine sediment deposits attributed mainly to a river discharge. The contribution of anomalous density heterogeneities within the consolidated crust is mostly negative over the oceanic crust, while positive inland including continental margins. Maxima of this contribution up to about 2.5 E along the central and southern Andes are separated from positive values over cratons and intracratonic basins of eastern South America by negative values along continental basins east of Andes.

7.2.4 Moho and elastic lithospheric thickness models

The lithospheric elastic thickness model used here was computed by Tassara *et al.* (2007) by applying a wavelet-based method for the Bouguer gravity data and topography inversion by means of a spectral coherence. The result is shown in Fig. 5(a). As seen, the lithospheric elastic thickness has a relatively smooth pattern with values typically below 20 km along the active Andean margin and the passive Atlantic margin, whereas the maximum value of 90 km is located at the core of the Brazilian Shield.

We applied the flexural theory for computing the Moho depth, while taking into consideration the variable Moho density contrast (Fig. 3) and the elastic thickness of the lithosphere (Fig. 5a). The spherical harmonic synthesis is done pointwise considering the elastic thickness and density contrast at any point. The regional Moho model (Fig. 5b) shows a typical pattern characterized by a significant contrast between thin oceanic and thick continental crust. The maximum Moho deepening under the Andes reaches roughly 70 km.

In order to compare the differences between the VMM and flexural Moho models, we performed a sensitivity analysis depending on the choice of the parameter of the lithospheric elastic thickness T_e. The statistical summary of differences between the VMM and flexural Moho models for different values of T_e is given in Table 1. As seen from the results, the mean value of differences remains the same (−2.5 km), while the root mean squares (rms) of differences vary only slightly (from 3.5 to 3.9 km). We also computed these differences for the model presented by Tassara *et al.* (2007). In this case, the differences are smallest. These results showed that differences between the flexural and VMM Moho models are not significant. The results of numerical analysis not presented here in detail revealed that these differences do not propagate significantly into the gravitational contribution of the crustal density heterogeneities

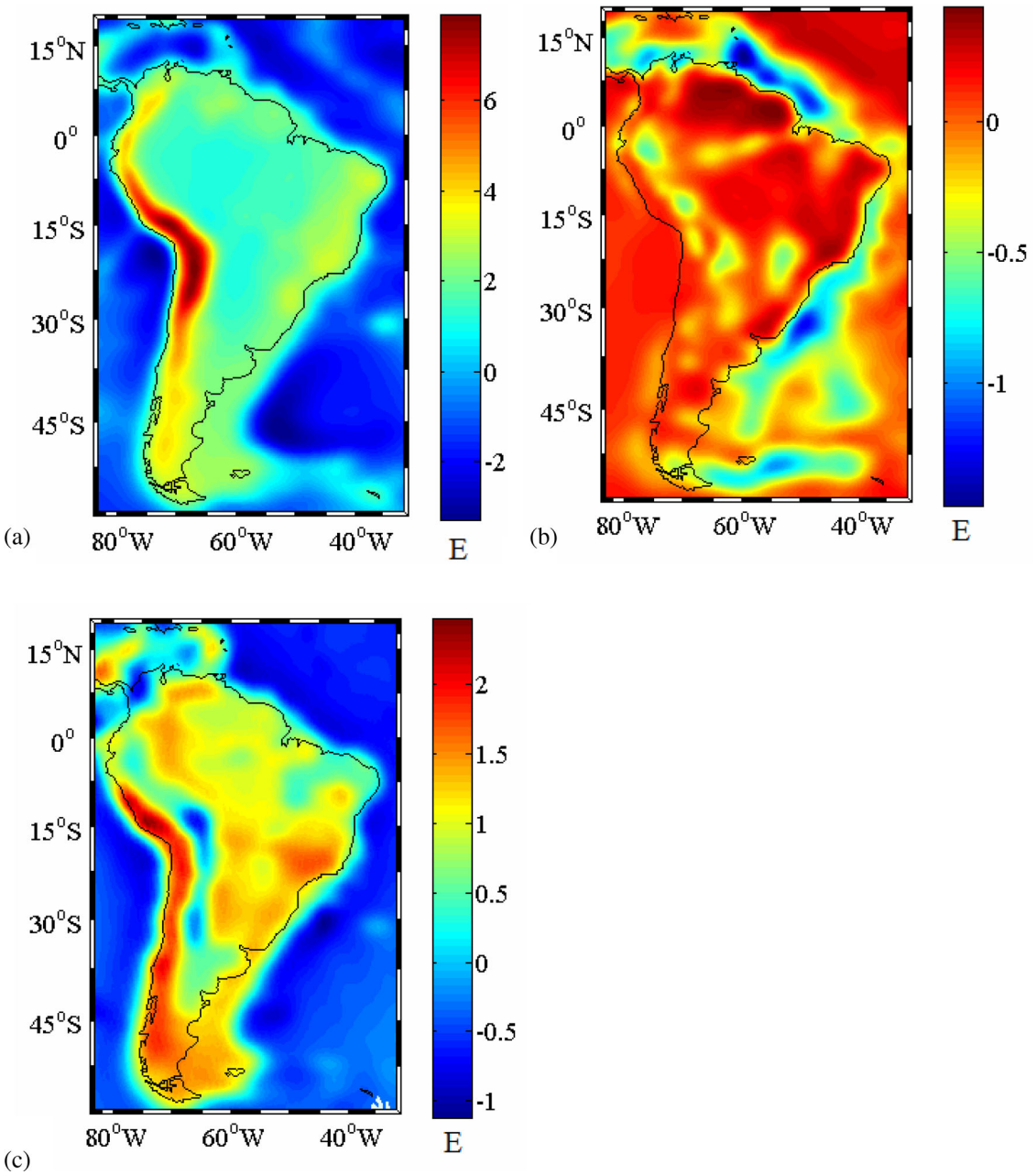

Figure 4. Contributions on the vertical gravitational gradient due to: (a) topography and bathymetry, (b) sediments and (c) consolidated crust.

and subsequently into the lithospheric stress. This is explained by the fact that these differences have mainly high-frequency character.

7.2.5 Contribution of crustal structure on gravitational gradient

The individual gravitational gradient contributions of topography, bathymetry, sediments and consolidated crust are rather large, but the topographic mass surplus, bathymetric mass deficiency as well as crustal density heterogeneities are compensated not only within the crust (variable crustal thickness), but also deeper within the subcrustal lithosphere. Here, we used the Moho model (shown in Fig. 5b) to apply the compensation effect on the gravitational gradient. This computation was done according to the expression in eq. (3c) by applying the contribution of the variable Moho density contrast and the lithospheric elastic thickness. As a result, the combined effect of these contributions is considerably smaller than the individual contributions, and also smaller than the gravity-gradient signal itself. The combined contribution from the topography, bathymetry, sediments and density heterogeneities within the remaining crust (down to and including the Moho interface) is shown in Fig. 6, with values mostly between −0.7 and 0.2 E. The isostatic signature of Andes marked by the largest negative values is flanked on both sides of the central Andes by large positive values along the subduction zone of the Nazca plate and the zone of convergence between the Altiplano and South American plates.

8 RESULTS

We applied the mantle flow (Hager and O'Connell) and gravimetric (Runcorn) solutions (Sections 4 and 5) to model the lithospheric

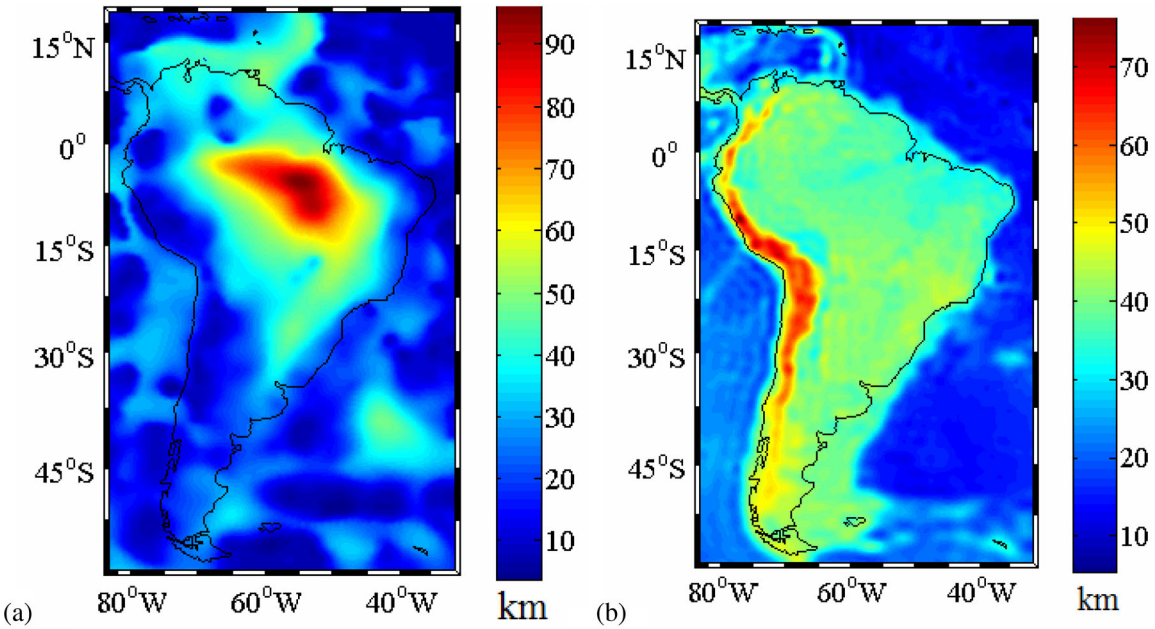

Figure 5. Regional maps of: (a) the elastic thickness of the lithosphere according to Tassara *et al.* (2007), and (b) the Moho depth.

Table 1. Sensitivity analysis of differences between the flexural and gravimetric Moho depths depending on the choice of lithospheric elastic thickness T_e.

T_e (km)	Max	Mean	Min	rms
0	10.0	−2.5	−13.8	3.6
5	9.7	−2.5	−13.5	3.6
10	8.2	−2.5	−12.3	3.6
15	7.1	−2.5	−12.8	3.5
20	7.4	−2.5	−13.7	3.5
25	8.6	−2.5	−14.6	3.5
30	9.7	−2.5	−15.4	3.5
50	12.6	−2.5	−18.2	3.5
90	15.2	−2.5	−21.2	3.9
Tassara *et al.*	**7.0**	**−2.5**	**−11.8**	**3.5**

stresses within the study area of South America. We then repeated the computation using the newly developed combined model (Section 6) and compared the results.

8.1 Lithospheric stress based on mantle flow solution

The lithospheric shear stresses at a constant depth of 100 km were taken from Steinberger *et al.* (2001, corresponding to their fig. 6d). 100 km depth is the base of the lithosphere in that model, which only considers radial viscosity variations. If variations of lithosphere thickness were considered, the stress pattern is expected to remain similar but with magnitudes somewhat changed, because, for example, for a thicker lithosphere, the coupling with underlying mantle flow is somewhat stronger. However, such effects were not considered here. The result is shown in Fig. 7. A plate velocity model was used to formulate the surface boundary conditions for solving the mantle-flow equations. However, plate velocities are not prescribed, but chosen such that plates move at half the speed (rotation rates) for which the forces acting at their bases would exactly be balanced. The viscosity structure features a 100-fold increase with depth and is consistent with geodynamic models of the geoid (e.g. Hager & Richards 1989) and the postglacial rebound (e.g. Lambeck & Johnson 1998). It is worth mentioning that the stresses do not considerably depend on the viscosity structure (*cf.* Steinberger *et al.* 2001). Also, since they are dominated by a large-scale mantle structure, they remain essentially similar if one updates to more recent tomography-derived mantle density models. The spherical harmonic series used for generating the stress field was truncated at degree of 31, which corresponds to the wavelength of about 1200 km and it is sufficient for modeling the long-wavelength lithospheric stress anomalies (*cf.*

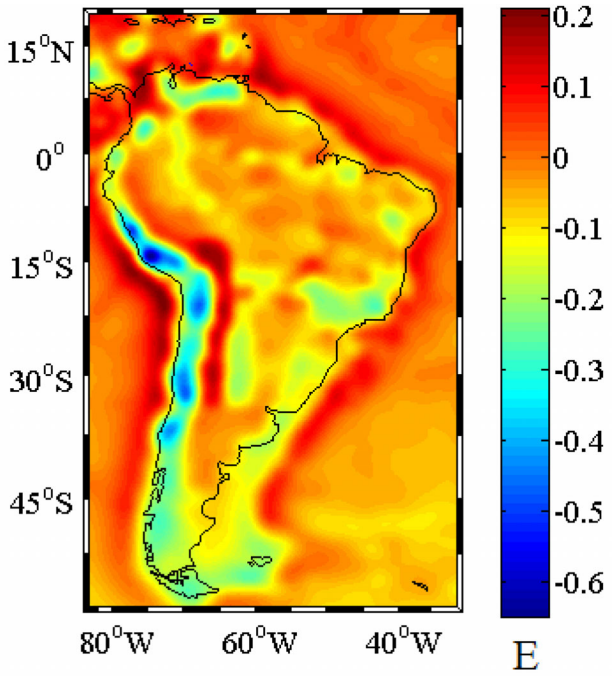

Figure 6. Combined contribution of crustal density heterogeneities and the Moho depth on the gravitational gradient.

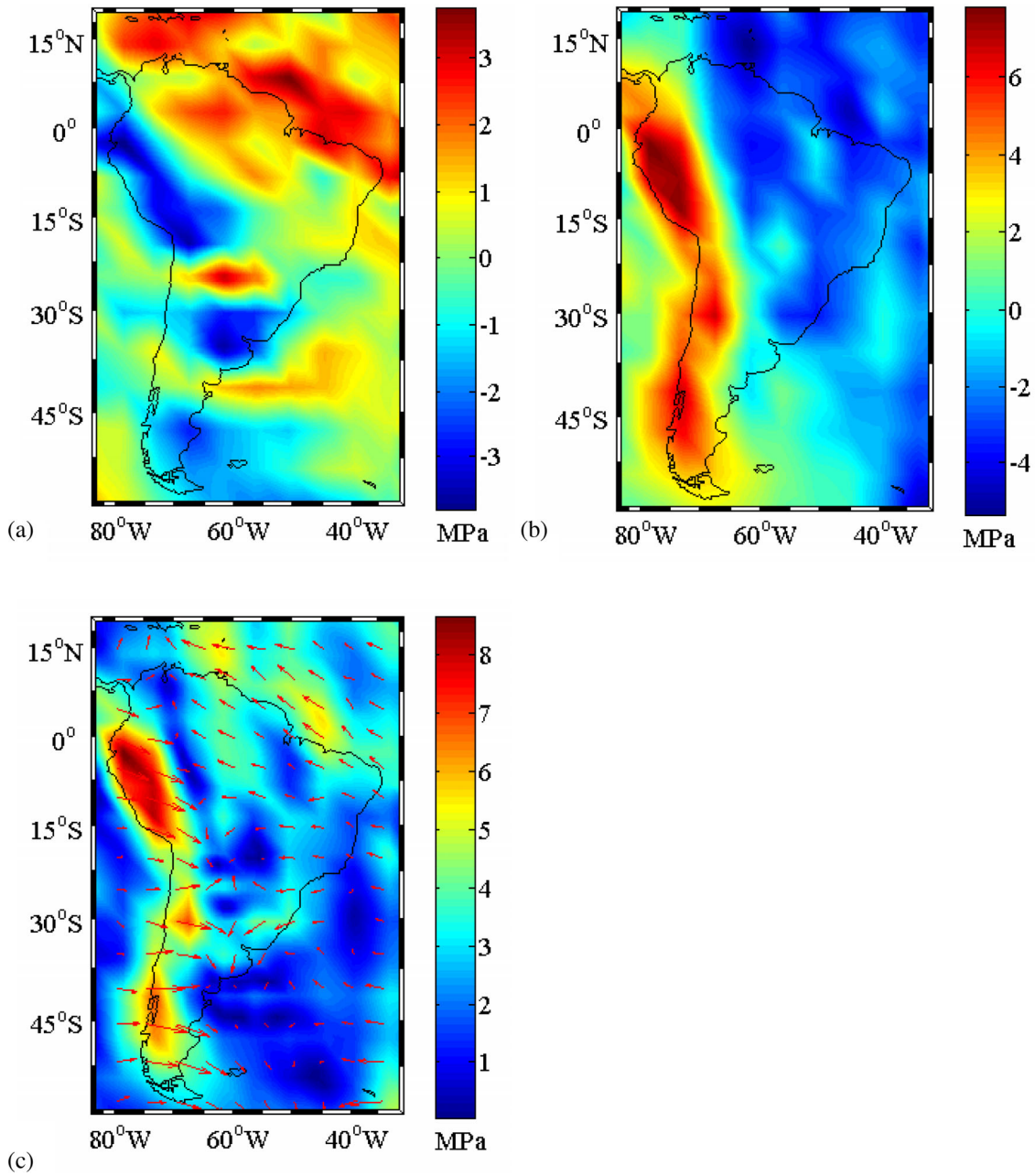

Figure 7. Regional map of stress field in South America derived by Steinberger *et al.* (2001) based on Hager and O'Connell's theory and the mantle density model that is inferred from an earlier version of Grand's (2002) tomography model: (a) the northward stress component, (b) the eastward stress component and (c) the stress-vector orientation and intensity.

Steinberger *et al.* 2001). It is worth mentioning here that changes in results due to using a higher degree resolution (above degree 31) are negligible.

The northward and eastward stress components are shown in Figs 7(a) and (b), respectively. Positive values in Fig. 7(a) represent the northward orientation, while negative values have the opposite (southward) orientation. Similarly, in Fig 7(b), positive values apply to the eastward orientation, while negative to the westward orientation. As seen in Fig. 7(c), the maximum stress intensity is detected below the Andean margin, distinctively marking its segmentation and presenting larger stresses along flat segments of the subsided Nazca slab. This stress distribution closely agrees with a mantle flow pattern within the study area. The stress vectors have a prevailing eastward orientation under the Nazca plate corresponding to its motion. Moreover, the eastward stress-vector orientation beneath the Altiplano plate agrees with its convergent motion relative to the South American plate. The stress-vector orientation under the Amazonian Shield together with intermediate old cratonic formations including São Francisco, Luis Alves, Alto Paraguay and Río de la Plata cratons is characterized by a prevailing westward orientation. These two principal stress-vector orientations within South America converge under the continental basins east of the Andes in agreement with the convergent flow related to a downwelling in the model.

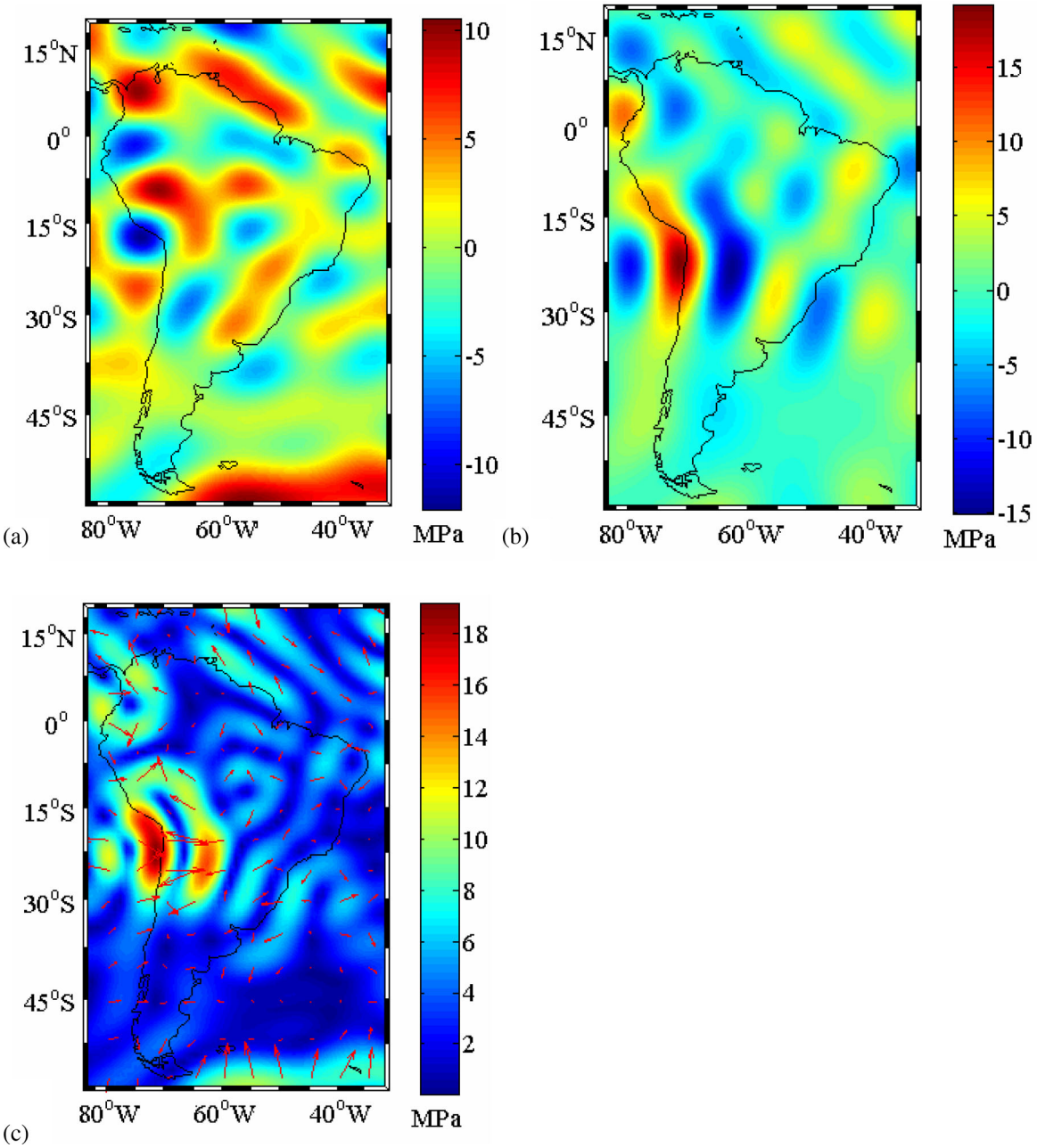

Figure 8. Regional map of stress field (MPa) in South America derived based on Runcorn's theory from the GOCE data (eq. 4a) uncorrected for the crust density heterogeneities: (a) the northward stress component, (b) the eastward stress component and (c) the stress-vector orientation and intensity.

8.2 Lithospheric stress based on gravimetric solution

We used the GOCE gravity-gradient data to model the stresses based on solving the integral equation in eq. (4e), after applying the spatial discretization on a 1 × 1 arcdeg grid corresponding to 4290 values over the study area. The computation was realized with the spectral kernel limited to degree of 31; see the integral kernel in eq. (4e) that in reality serves as a low-pass filter to GOCE data. Here, we inverted directly the GOCE data into the stress field without considering the crustal density heterogeneities. For computing the stress-generating function from the integral given in eq. (4e), this integral was discretized according to the used resolution of 1 × 1 arcdeg. In this way, we solved the system of equations for 21920 measurements and 4290 unknown values. Since the system of equations is ill conditioned, we applied Tikhonov's regularization to solve the inversion problem and remove higher frequencies that are contaminated by data errors in combination with the quasi-optimal method (Hansen 1998) that was used for a determination of the regularization parameter. The obtained values of the stress-generating function S_r were then converted to the northward and eastward stress components by applying a numerical differentiation; see eqs (6f) and (6g). The result is shown in Fig. 8.

As seen in Fig. 8(c), the stress pattern in this case coincides more closely with tectonic plate boundaries, thus reflecting mainly a tectonic response to mantle flow. The maximum stress intensity is detected along two convergent tectonic margins, namely between the Nazca and Altiplano plates and between the Altiplano and South American plates. A prevailing convergent stress-vector orientation

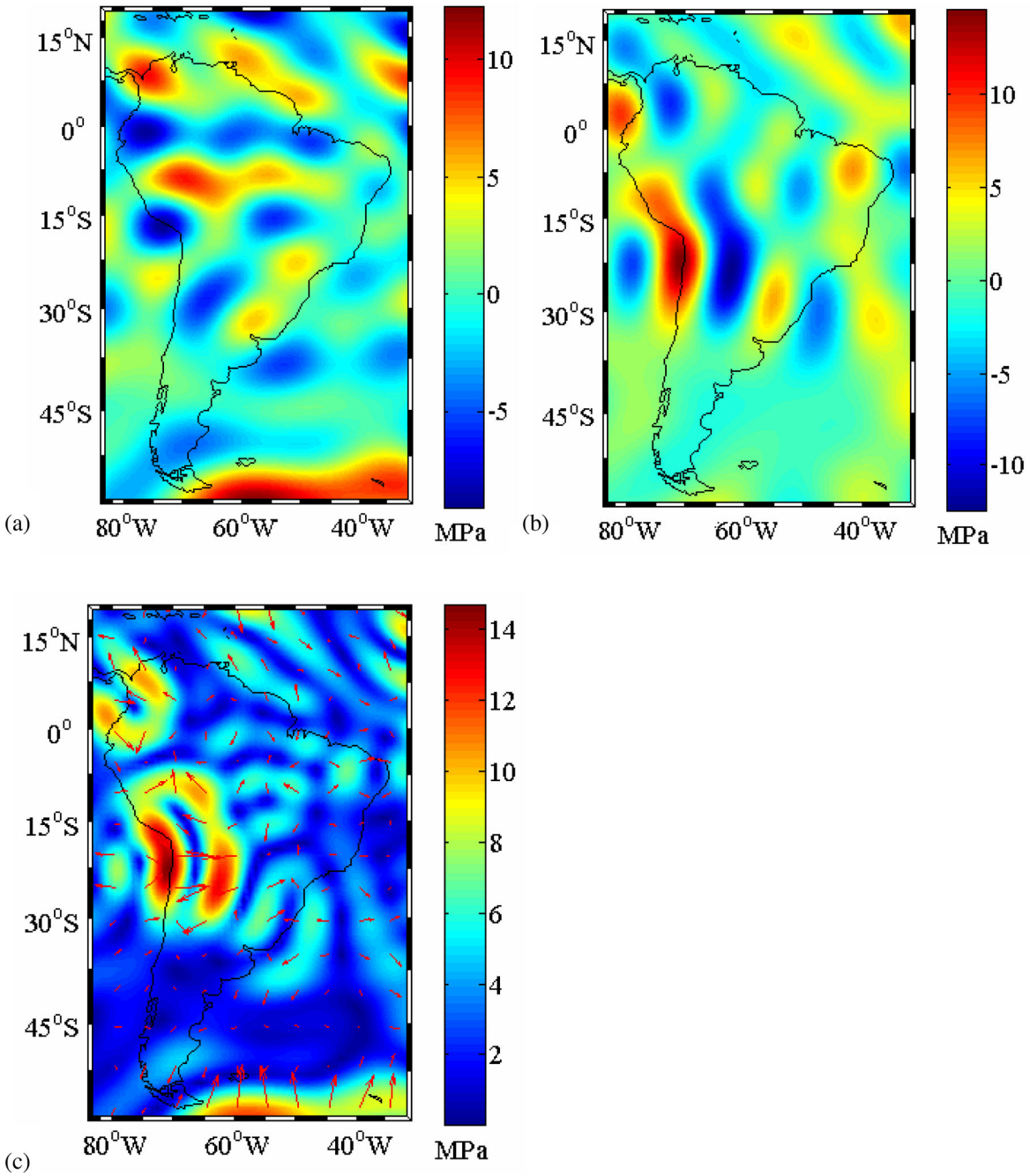

Figure 9. Regional map of stress field in South America derived based on Runcorn's theory from the GOCE data (eq. 4a) corrected for the contributions of topography and crustal density heterogeneities: (a) the northward stress component, (b) the eastward stress component and (c) the stress-vector orientation and intensity.

along central Andes agrees with the compressional tectonism of orogenic formations. This stress pattern indicates that the estimation of the stress field from the uncorrected GOCE data reflects more shallow stresses. Elsewhere, the stress intensity is relatively small. Overall, maximum stress intensity occurs in tectonically active regions, while old, stable cratons are characterized by the lower stress magnitude.

We further took into consideration the effect of crustal density heterogeneities. For this purpose, we modeled the contributions of topography and density contrasts of bathymetry, sediments and consolidated crust, and subtracted them from the GOCE data. Furthermore, we computed and subtracted the compensation effects of these contributions according to the flexural model of isostasy. In this way, the spatial distribution of S_r becomes smoother, thus reducing the intensity of the resulting stress field (compared to the result from the uncorrected GOCE data). The stress field obtained from the GOCE data corrected for the contributions of topography and crustal density heterogeneities is shown in Fig. 9. By comparing Figs 8(c) and 9(c), the overall spatial pattern of the stress field does not change considerably, but the stress intensity decreased (by up to about 4 MPa) after applying these corrections, especially on both sides of the central Andes. Such reduction in the stress intensity was

expected due to removing the lithospheric stress signature. Overall, however, the stress field computed (for the corrected as well as uncorrected GOCE data) according to Runcorn's theory reflects more likely stresses attributed to a tectonic respond of the lithosphere to mantle flow.

8.3 Lithospheric stress based on combined gravimetric and mantle flow solutions

The maximum stress intensity computed according to Runcorn's theory reaches about 18 MPa (*cf.* Fig. 8c). After reducing the GOCE data for the contributions of topography and crustal density heterogeneities, this value reduced down to about 14 MPa (*cf.* Fig. 9c). In contrast, the maximum stress intensity inferred from the mantle flow solution is only about 8 MPa (*cf.* Fig. 7c). From the spectrum of S_r (eq. 4d), we can see that the series is not convergent as there is an amplifying factor of $(R/(R-D))^{n+1}$ which magnifies higher frequencies of the solution when degrees increase. In fact, by organizing integral equations and solving their discretized form, the problem of divergence and ill-conditioning of the system are mixed and by the regularization both of them are solved simultaneously. However, the regularization is a mathematical technique and it is not clear how meaningful the result is. In such a case, some other constraining parameters are needed. Phillips & Ivins (1979) have mentioned that combining Runcorn's solutions with other geological parameters is required to compensate for oversimplifications done by Runcorn.

Following this idea, we jointly inverted the GOCE data (corrected for the crustal density heterogeneities) and the mantle flow equations for the shear stresses in order to estimate S_r. The system of discretized equations (eq. 6h) was formed for 21920 GOCE gravity gradients and 4290 values of the stress-generating function. The system of equations further involved the stress components generated according to the mantle flow equations as additional observations. However, it is important to clarify that the unknown parameters in our system are S_r, not the stress components. Hence, the stress components are connected to S_r via eqs (6f) and (6g). The mantle flow solution provided 4290 values of the northward and eastward stress components. In this way, we added extra 8580 observations into our system, so that the total number of observations increased to 30500, while the number of unknowns (4290) remain the same. By combining the GOCE data inversion with the mantle flow solution, the system becomes stable and well conditioned, so that a simple least-squares analysis provided the combined solution directly. The result of this combination is shown in Fig. 10. As seen from the results in Figs 7 and 10, the combined solution very closely resembles the mantle flow solution, expect for some minor differences mainly related to lessened stress intensity under the central and southern Andes. The mantle flow solution thus contributes much more into the combined solution than the GOCE data inversion. We explain this by an instability of the system of equations formed only for the GOCE data inversion.

9 SUMMARY AND CONCLUDING REMARKS

We have compared methods for the lithospheric stress modeling based on gravimetric (Runcorn's) and mantle flow (Hager and O'Connell's) solutions. We further developed and applied the combined method based on the gravity data (in our case the GOCE vertical gravity gradients) inversion by means of a least-square analysis constrained by the mantle flow equations according to Hager and O'Connell. The application of these constraining parameters stabilized the GOCE data inversion, so that the regularization was not needed. The GOCE vertical gravity gradients used for this purpose were corrected for the gravitational contribution of crustal density heterogeneities in order to reveal the gravitational signature of the mantle. The mathematical model used for estimating the gravitational contribution of crustal density heterogeneities was developed based on combining the VMM and flexural models of isostasy, while assuming that both models provide the same Moho result.

The comparison of results over the study area of South America revealed that the mantle flow solution reflects mainly the lithospheric stresses due to mantle flow, while the gravimetric solution reflects a tectonic response of the lithosphere to mantle flow. Moreover, the combined solution agrees very closely with the mantle flow solution in terms of the stress pattern and its intensity. The main difference between these two solutions is slightly lower stress intensity in the combined solution under orogenic regions of the central and southern Andes. In contrast, relatively large differences were found between the combined and gravimetric solutions, with very different stress pattern as well as stress intensity. The most significant differences were at locations of the maximum stress intensity which according to the combined (as well as mantle flow) solution was detected under the northern part of the Central Andes of Peru, while stress recovery from GOCE data according to Runcorn's theory showed the maximum stress intensity along the subduction zone between the Nazca and Altiplano plates and further east along the convergent tectonic margin between the Altiplano and South American plates. In contrast, the stress pattern inferred according to the combined model, as dominated by the Hager and O'Connell's solution and therefore by the mantle circulation model, is strongly correlated with the position of flat-slab segments of the subsided Nazca plate. Indeed, when comparing the geological configuration (Fig. 1) with the stress distribution (Fig. 10), it becomes clear that the region where horizontal stresses are greater than 6 MPa underneath Peru (0°–18°S) is characterized by a large flat-lying segment of the Nazca slab between 150 and 300 km depth, which itself is associated with a gap of the volcanic arc and northward decreasing elevations of the Cordillera. A similar spatial correlation can be established between a region of relatively large intensity of horizontal stresses (4–6 MPa) in the western part of Argentina (between approximate 25°S and 33°S) and the location of the Pampean flat-slab segment with its associated volcanic gap (Fig. 1). In both cases, the eastward motion of the Nazca slab at shallow depths under the South-American lithosphere is likely dragging the continental plate and pushing it towards the east, explaining the greater distance from the trench that current crustal deformation has in these regions compared to segments where the slab dip is normal (e.g. Ramos 1999). In addition, the nuclei of Archean to Palaeoproterozoic cratons also show relatively large amplitudes of horizontal stresses in our combined model, with vector directions towards the west, implying that upper-mantle circulation from the Atlantic ridge is actively dragging the keel of these cratons and therefore the whole continent toward the trench.

A very close agreement between the combined and mantle flow solutions indicates that the observation equations related to the mantle flow solution represent a more significant contribution to the final stress solution, while the number of mantle flow equations is lower than the number of observation equations used for the GOCE data inversion. However, including the mantle flow solution as additional observation equations into our system can control the instability of the system based on Runcorn's theory so that a

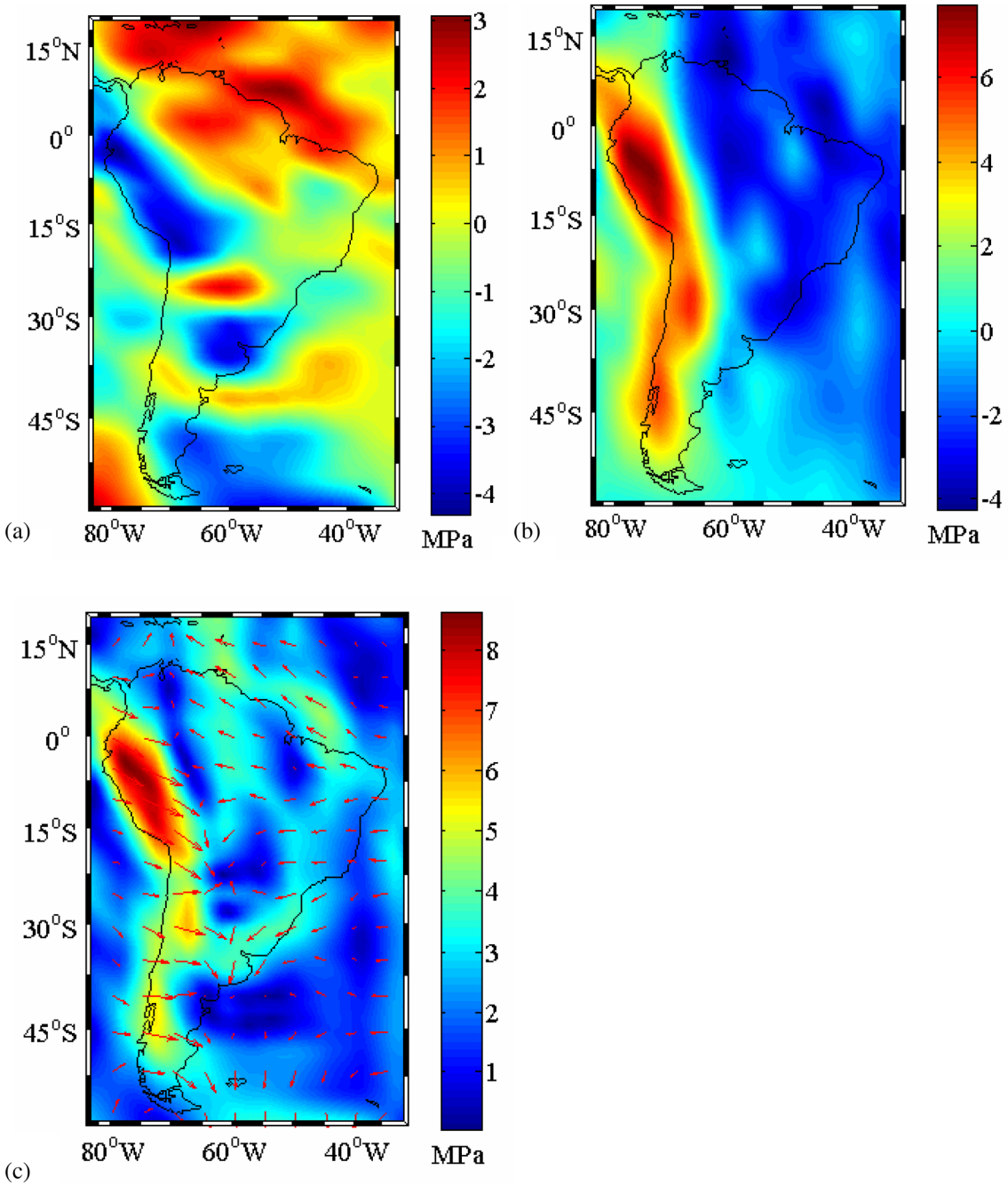

Figure 10. Regional map of stress field (MPa) in South America derived from the GOCE data corrected for crustal density heterogeneities and based on combining Runcorn's and Hager and O'Connell's theories for the mantle flow model: (a) the northward stress component, (b) the eastward stress component and (c) the stress-vector orientation and intensity.

regularization is no longer required for solving the equations. Due to this instability, the combined solution agrees more closely with the mantle flow solution. The GOCE data information from Runcorn's theory can be used to determine the stress field in regions where data used for the mantle flow solution are sparse or absent.

ACKNOWLEDGEMENTS

The authors are thankful to Prof Bert Vermeersen and anonymous reviewers for their constructive comments.

REFERENCES

Abrehdary, M., 2016. Recovering moho parameters using gravimetric and seismic data, *PhD dissertation*, Royal Institute of Technology (KTH), Stockholm, Sweden.

Assumpçao, M., Schimmel, M., Escalante, C., Roberto Barbosa, J., Rocha, M. & Barros, L.V., 2004. Intraplate seismicity in SE Brazil: stress concentration in lithospheric thin spots, *Geophys. J. Int.*, **159**(1), 390–399.

Bird, P., 2003. An updated digital model of plate boundaries, *Geochem. Geophys. Geosyst.*, **4**(3), 3, doi:10.1029/2001GC000252.

Braitenberg, C., Ebbing, J. & Götze, H.J., 2002. Inverse modelling of elastic thickness by convolution method - the eastern Alps as a case example, *Earth planet. Sci. Lett.*, **202**(2), 387–404.

Cordani, U.G. & Sato, K., 1999. Crustal evolution of the South American Platform, based on Nd isotopic systematics on granitoid rocks, *Episodes-Newsmag. Int. Un. Geol. Sci.*, **22**(3), 167–173.

Eshagh, M., 2014. From satellite gradiometry data to subcrustal stress due to mantle convection, *Pure appl. Geophys.*, **171**(9), 2391–2406.

Eshagh, M., 2016. On Vening Meinesz-Moritz and flexural theories of isostasy and their comparison over Tibet Plateau, *J. Geod. Sci.*, **6**(1), 139–151.

Eshagh, M., 2017. On the approximations in formulation of the Vening Meinesz-Moritz theory of isostasy, *Geophys. J. Int.*, **210**(1), 500–508.

Eshagh, M. & Hussain, M., 2016. An approach to Moho discontinuity recovery from on-orbit GOCE data with application over Indo-Pak region, *Tectonophysics*, **690**, 253–262.

Farr, T.G. *et al.*, 2007. The shuttle radar topography mission, *Rev. Geophys.*, **45**(2), RG2004, doi:10.1029/2005RG000183.

Fu, R. & Huang, P., 1983. The global stress field in the lithosphere obtained from the satellite gravitational harmonics, *Phys. Earth planet. Inter.*, **31**(3), 269–276.

Gladkikh, V. & Tenzer, R., 2011. A mathematical model of the global ocean saltwater density distribution, *Pure appl. Geophys.*, **169**(1–2), 249–257.

Grand, S.P., 2002. Mantle shear-wave tomography and the fate of subducted slabs, *Phil. Trans. R. Soc. Lond., A: Math. Phys. Eng. Sci.,* **360,** 2475–2491.

Hager, B.H. & Richards, M.A., 1989. Long-wavelength variations in Earth's geoid: physical models and dynamical implications, *Phil. Trans. R. Soc. A: Math. Phys. Eng. Sci.*, **328**(1599), 309–327.

Hager, B.H. & O'Connell, R.J., 1981. A simple global model of plate dynamics and mantle convection, *J. geophys. Res.*, **86**(B6), 4843–4867.

Hansen, P.C., 1998. *Rank-Deficient and Discrete Ill-Posed Problems: Numerical Aspects of Linear Inversion*, SIAM, Philadelphia.

Hinze, W.J., 2003. Bouguer reduction density, why 2.67?, *Geophysics*, **68**(5), 1559–1560.

Kaula, W.M., 1963. Elastic models of the mantle corresponding to variations in the external gravity field, *J. geophys. Res.*, **68**(17), 4967–4978.

Kraus, H., 1967. *Thin Elastic Shells: An Introduction to the Theoretical Foundations and the Analysis of Their Static and Dynamic Behavior*, p. 476, John Wiley, New York.

Lambeck, K. & Johnson, P., 1998. The viscosity of the Mantle: evidence from analyses of glacial-rebound phenomena, in *The Earth's Mantle*, pp. 461–502, ed. Jackson, I., Cambridge University Press, Cambridge.

Laske, G., Masters, G., Ma, Z. & Pasyanos, M.E., 2013. Update on CRUST1.0—a 1-degree global model of Earth's crust, Geophysical Research Abstracts 15 (**Abstract EGU2013-2658**).

Liu, H.S., 1977. Convection pattern and stress system under the African plate, *Phys. Earth planet. Inter.*, **15**(1), 60–68.

Liu, H.S., 1978. Mantle convection pattern and subcrustal stress field under Asia, *Phys. Earth planet. Inter.*, **16**(3), 247–256.

Marsh, B.D. & Marsh, J.G., 1976. On global gravity anomalies and two-scale mantle convection, *J. geophys. Res.*, **81**(29), 5267–5280.

McKenzie, D.P., 1967. Some remarks on heat flow and gravity anomalies, *J. geophys. Res.*, **72**(24), 6261–6273.

McNutt, M., 1980. Implications of regional gravity for state of stress in the Earth's crust and upper mantle, *J. geophys. Res.*, **85**(B11), 6377–6396.

Medvedev, S., 2016. Understanding lithospheric stresses: systematic analysis of controlling mechanisms with applications to the African Plate, *Geophys. J. Int.*, **207**(1), 393–413.

Moritz, H., 2000. Geodetic reference system 1980, *J. Geod.*, **74**(1), 128–133.

Müller, R.D., Roest, W.R., Royer, J.Y., Gahagan, L.M. & Sclater, J.G., 1997. Digital isochrons of the world's ocean floor, *J. geophys. Res.*, **102**(B2), 3211–3214.

Phillips, R.J. & Ivins, E.R., 1979. Geophysical observations pertaining to solid-state convection in the terrestrial planets, *Phys. Earth planet. Inter.*, **19**(2), 107–148.

Ramos, V., 1999. Plate tectonic setting of the Andean Cordillera, *Episodes*, **22**, 183–190.

Rexer, M., Hirt, C., Claessens, S. & Tenzer, R., 2016. Layer-based modelling of the Earth's gravitational potential up to 10-km scale in spherical harmonics in spherical and ellipsoidal approximation, *Surv. Geophys*, **37**(6), 1035–1074.

Ricard, Y., Fleitout, L. & Froidevaux, C., 1984. Geoid heights and lithospheric stresses for s dynamic Earth, *Ann. Geophys.*, **2**, 267–286.

Richards, M.A. & Hager, B.H., 1984. Geoid anomalies in a dynamic Earth, *J. geophys. Res.*, **89**(B7), 5987–6002.

Runcorn, S.K., 1964. Satellite gravity measurements and a laminar viscous flow model of the Earth's mantle, *J. geophys. Res.*, **69**(20), 4389–4394.

Runcorn, S.K., 1967. Flow in the mantle inferred from the low degree harmonics of the geopotential, *Geophys. J. R. astr. Soc.*, **14**(1–4), 375–384.

Sjöberg, L.E., 2009. Solving Vening Meinesz-Moritz inverse problem in isostasy, *Geophys. J. Int.*, **179**(3), 1527–1536.

Steinberger, B., Schmeling, H. & Marquart, G., 2001. Large-scale lithospheric stress field and topography induced by global mantle circulation, *Earth planet. Sci. Lett.*, **186**(1), 75–91.

Stewart, J. & Watts, A.B., 1997. Gravity anomalies and spatial variations of flexural rigidity at mountain ranges, *J. geophys. Res.*, **102**(B3), 5327–5352.

Tassara, A., Swain, C., Hackney, R. & Kirby, J., 2007. Elastic thickness structure of South America estimated using wavelets and satellite-derived gravity data, *Earth planet. Sci. Lett.*, **253**(1–2), 17–36.

Tenzer, R., Novák, P., Vajda, P., Gladkikh, V. & Hamayun, 2012. Spectral harmonic analysis and synthesis of Earth's crust gravity field, *Comput. Geosci*, **16**(1), 193–207.

Tenzer, R., Chen, W., Tsoulis, D., Bagherbandi, M., Sjöberg, L.E., Novák, P. & Jin, S., 2015. Analysis of the refined CRUST1.0 crustal model and its gravity field, *Surv. Geophys.*, **36**(1), 139–165.

Tikhonov, A.N., 1963. Solution of incorrectly formulated problems and regularization method, *Soviet Math. Dokl.*, 4, 1035–1038. [English translation of DokladyAkademiiNauk SSSR, **151**, 501–504.]

Turcotte, D.L. & Schubert, G., 1982. *Geodynamics: Applications of Continuum Physics to Geological Problems*, p. 450, John Wiley & Sons, New York.

Turcotte, D. & Schubert, G., 2014. *Geodynamics*, 3rd edn, Cambridge University Press.

Vening Meinesz, F.A., 1931. Une Nouvelle méthode pour la reduction isostatique régionale de L'intensité de la Pesanteur, *Bull.Géod.*, **29**, 33–51.

Watts, A.B., 2001. *Isostasy and Flexure of the Lithosphere*, Cambridge University Press.